scientific reports

Check for updates

OPEN

Comparative simulation analysis of photonic ultrasound sensors based on silicon waveguides

Tabea Fünning[1]✉, Martin Paul[2], Costanza Lucia Manganelli[1], Christian Wenger[1,3], Andreas Mai[1,2] & Patrick Steglich[1,2]

Pressure sensors based on photonic integrated circuits (PIC) offer the prospect of outstanding sensitivities, extreme miniaturization and have the potential for highly scalable production using CMOS compatible processing. PIC-based pressure sensors detect the change in optical properties, i.e. the intensity or phase of the optical carrier wave inside miniaturized waveguide structures. The detection of ultrasound is achieved by engineering the waveguide architecture such that a pressure causes a high change in the effective refractive index of the waveguide. A range of PIC-based pressure sensors have been reported, but a comparison of the sensitivity of the different approaches is not straightforward, since different pressure sensitive waveguide architectures as well as photonic layouts and measurement setups impact the performance. Additionally, the used sensitivity unit is not uniform throughout the different studies, further complicating a comparison. In this work, a detailed simulation study is carried out by finite element modeling of different pressure sensitive waveguide architectures for a consistent comparison. We analyze three different sensor architectures: (A) a free standing membrane located within a tiny air gap above the waveguide, (B) a waveguide located on top of a deflectable membrane as well as (C) a waveguide embedded inside a pressure-sensitive polymer cladding. The mechanical response of the structures and the resulting changes in mode propagation, i.e. the change of the effective refractive index, are analyzed. The waveguide sensitivities in RIU/MPa for different waveguide types (strip, slot) and polarization states (TE, TM) are compared. The results reveal inherent limitations of the different waveguide designs and create a basis for the selection of suitable designs for further ultrasound sensor development. Possibilities for enhancing waveguide sensitivity are identified and discussed. Additionally, we have shown that the studied approaches are extensible to SiN waveguides.

Ultrasound imaging is an established technique in biomedical diagnostics. Traditional sonography is carried out using piezoelectric transducers. The small bandwidth of the reflected ultrasound pulse is efficiently detected as the signal is produced and detected with the same device. Conversely, emerging technologies come along with different requirements regarding the ultrasound sensor specifications. A well known example is photoacoustic imaging. This biomedical imaging method relies on the photoelastic effect. Laser pulses are directed into biological tissue, where a fraction of the energy is absorbed and converted into heat. This phenomenon triggers a momentary thermoelastic expansion, leading to the release of broad-spectrum (i.e., MHz) ultrasonic waves. Subsequently, the ultrasound sensor captures and detects these generated ultrasonic waves. The drawbacks of piezoelectric sensors, i.e. their loss of sensitivity with reduced sensor size and limited bandwidth, are hindering such emerging technologies.

Optical sensors show a great potential in overcoming the current limitations of piezoelectric sensors by higher signal-to-noise ratio per unit area and wider detection bandwidths.[1] Different optical ultrasound sensors are researched including free-space optics[2–4], fiber based sensing[5,6], and photonic integrated circuits (PICs). The latter was primarily shown for polymer waveguides[7–10] but recently also demonstrated in silicon-based waveguides. PICs have great advantages over free-space optics because they can be produced with scalable manufacturing processes and offer the possibility of extreme miniaturization.

The first ultrasound sensor based on the SOI platform was shown by Rosenthal et al.[11] in 2014. A silicon waveguide architecture embedded into a SiO_2 cladding interrogated as a π-phase-shifted Bragg-grating is used for sensing. The sensor shows a response dominated by the formation of surface acoustic waves (SAW). Since

[1]IHP - Leibniz-Institute for High Performance Microelectronics, Frankfurt(Oder) D-15236, Germany. [2]Technische Hochschule Wildau, Wildau D-15745, Germany. [3]Brandenburgische Technische Universität (BTU) Cottbus-Senftenberg, 03046 Cottbus, Germany. ✉email: fuenning@ihp-microelectronics.com

then, different approaches were proposed and experimentally demonstrated to avoid signal distortion by SAW and enhance sensitivity. A resonant SiO_2 membrane with a silicon waveguide on top of the membrane was shown by Leinders et al.[12] The deformation of the membrane and waveguide lead to a stress-induced refractive index change in the materials. A footprint of 124 µm, a sensitivity of 2.1 mV/Pa and a NEP of 0.4 Pa were demonstrated for an acoustic resonance frequency of 0.76 MHz. A sensor array with a full BEOL was proven feasible for this approach by Zarkos et al.[13] In the study of Westerveld et al.[14] a resonant membrane is placed with a tiny gap above a waveguide, while the waveguide is fixed onto a substrate. As the electric field intensity of the waveguide mode is high inside this gap, a slight, ultrasound-induced change in the gap height results in a large change in the effective refractive index of the waveguide. A NEP below 1.3 $\mathrm{mPaHz}^{1/2}$ was demonstrated for a bandwidth of 3-30 MHz and a wavelength shift of 35 fmPa^{-1} at an ultrasound frequency of 26 MHz for a MRR with a 5.5µm radius and a membrane diameter of 20 µm. A different approach is the use of a polymer cladding applied on top of the waveguide. Polymers with a strong photoelastic response allow evanescent field sensing. This was shown for example by Ding et al.[15] using a silicon waveguide with a SU-8 photoresist cladding. For a 10 µm MRR radius a NEP of 14.5 $\mathrm{mPaHz}^{1/2}$ and a 6 dB bandwidth of 165 MHz was reported. Nagli et al.[16] used polydimethylsiloxane (PDMS) as a cladding material and demonstrated a NEP of 7 $\mathrm{mPaHz}^{1/2}$ and a bandwidth of 120 MHz for a silicon nitride MRR with a diameter of 30 µm. A wavelength shift of 0.9 pmkPa^{-1} was measured in the optical C-band.

In the majority of studies the sensitivity of the final ultrasound sensor is reported, which depends on the waveguide sensitivity, the photonic layout as well as the measurement set-up. Comparing the waveguide sensitivity of the different approaches is not straightforward. However, to select a suitable approach for the design of a photonic ultrasound sensor, approximate values of waveguide sensitivity are required together with other limiting factors like the waveguide losses, the critical bend radii and the integration complexity. This work focuses on optimizing waveguide sensitivities of the main pressure sensitive waveguide approaches and comparing their values in RIU/MPa. Moreover, sensitivity values for MRR configurations that allow for a device footprint of 20 µm will be discussed.

The approaches under consideration are shown in Fig. 1. The first approach (A) consists of a flexible silicon dioxide membrane with a thin amorphous silicon layer on its lower side, placed above the waveguide structure. This approach was demonstrated by Westerveld et al.[14] by waferbonding of the membrane onto the photonic structure using oxide spacers. The membrane consisted of a 2 µm thick low-stress SiO_2 mechanical layer and a 60 nm thick amorphous silicon optical layer.

In the second approach (B), a waveguide is placed on top of a silicon dioxide (BOX - buried oxide) membrane, as first shown by Leinders et al.[12], who used deep reactive ion etching for substrate opening on chip level. The BOX layer forms in this case a membrane, which can deform a photonic micro-ring resonator sensor.

Finally, the third approach (C) facilitates a polymer cladding on top of the waveguide, as demonstrated by Nagli et al.[16] using PDMS as the cladding material. PDMS is chosen, due to its high photoacoustic interaction, high transparency[17] and its high stability and easy bonding with silicon.

While past work has focused mainly on the strip waveguide geometry with quasi-TE polarized light, this study takes into account the quasi-TE as well as the quasi-TM mode (further named TE and TM mode) for all three approaches. For approach B and C the geometries of a strip and a slot waveguide are also investigated.

SOI is often used for the design of photonic ultrasound sensors, due to its advantage of strong field confinement allowing extreme miniaturization. In the field of photonic sensing, silicon nitride based systems are also an emerging technology, where the silicon waveguide core is exchanged by silicon nitride. Silicon nitride based ultrasound sensors were for example shown in the study of Nagli et al.[16] For a comparison of both material

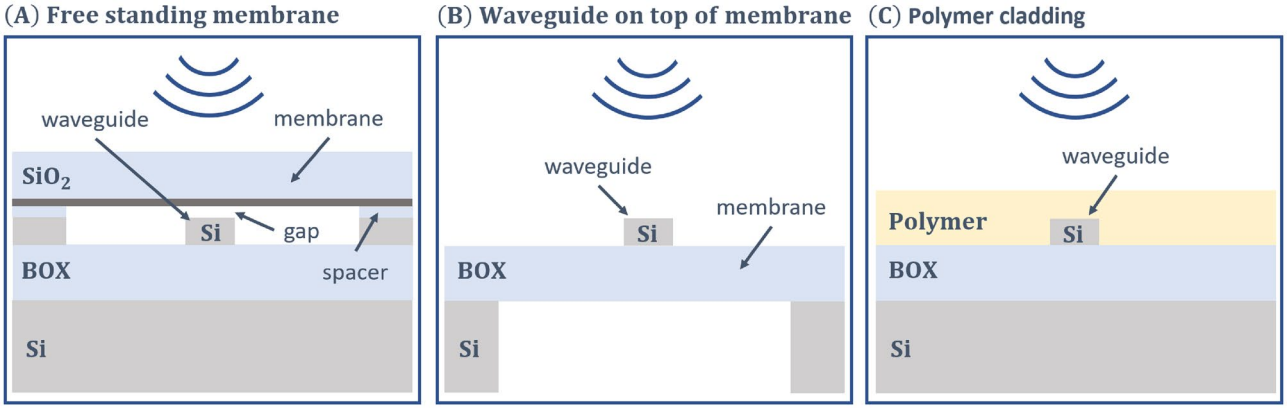

Fig. 1. Schematic illustration (not to scale) of the three design approaches considered within this study. A waveguide positioned on a Silicon-on-Insulator platform on top of the buried oxide layer (BOX) below a deflectable membrane (**A**) leads to a geometrical change once a pressure is applied. A waveguide on top of a deflectable membrane (**B**) leads to the photoelastic effect inside of silicon as well as silicon dioxide. Both mechanisms change the effective refractive index of the waveguide structure. A silicon waveguide with a polymer cladding (**C**) leads to a refractive index change mainly inside the polymer cladding due to a strong photoelastic interaction.

systems for each waveguide approach, the study (based on SOI devices) is repeated with silicon nitride. Detailed results for silicon nitride based approaches can be found in the appendix (Figures S1-S6).

Theory

The origin of the effective refractive index change due to external pressure is briefly summarized for the three different approaches.

Approach (A) employs a free-standing membrane above the waveguide. In this case, the effective index change $\partial n_e/\partial P$ is achieved by a slight variation in gap height g once the pressure P above the membrane changes:

$$\frac{\partial n_e}{\partial P} = \frac{\partial n_e}{\partial g} \cdot \frac{\partial g}{\partial P} \tag{1}$$

The change in gap height with the applied pressure $\partial g/\partial P$ depends on the membrane design (i.e. membrane material, thickness and diameter) and the radial displacement of the waveguide below the membrane. The membrane deflection for an exemplary membrane design is calculated and used throughout the study. The sensitivity $\partial n_e/\partial g$ is dependent on the waveguide geometry as well as the membrane thickness and the initial gap height g between the waveguide and the membrane.

Unlike (A), the approaches (B) and (C) rely on the photoelastic effect. For a waveguide on a membrane (B) as well as a waveguide with polymer cladding (C) the effective refractive index change $\partial n_e/\partial P$ is caused by the stress σ:

$$\frac{\partial n_e}{\partial P} = \frac{\partial n_e}{\partial \sigma} \cdot \frac{\partial \sigma}{\partial P} \tag{2}$$

Concerning the membrane-based design (B), the introduced stress $\partial\sigma/\partial P$, is again dependent on the membrane architecture as well as the radial displacement of the waveguide on top of the membrane surface. In contrast, the polymer cladding in approach (C) assures a separation between optical and acoustical design. The sensitivity $\partial n_e/\partial\sigma$ depends on the photoelastic properties of the material, which are described below.

The photoelastic effect is described by the strain S_j induced change of the impermeability $\Delta\eta_i$:

$$\Delta\eta_i = \Delta\left(\frac{1}{n^2}\right)_i = p_{ij}S_j \tag{3}$$

Inserting the strain-optic tensor for a cubic crystal structure (Si, SiO_2) leads to:[18]

$$\begin{bmatrix} \Delta\eta_1 \\ \Delta\eta_2 \\ \Delta\eta_3 \\ \Delta\eta_4 \\ \Delta\eta_5 \\ \Delta\eta_6 \end{bmatrix} = \begin{bmatrix} p_{11} & p_{12} & p_{12} & 0 & 0 & 0 \\ p_{12} & p_{11} & p_{12} & 0 & 0 & 0 \\ p_{12} & p_{12} & p_{11} & 0 & 0 & 0 \\ 0 & 0 & 0 & p_{44} & 0 & 0 \\ 0 & 0 & 0 & 0 & p_{44} & 0 \\ 0 & 0 & 0 & 0 & 0 & p_{44} \end{bmatrix} \begin{bmatrix} S_1 \\ S_2 \\ S_3 \\ S_4 \\ S_5 \\ S_6 \end{bmatrix} \tag{4}$$

And for an isotropic structure (polymer):

$$\begin{bmatrix} \Delta\eta_1 \\ \Delta\eta_2 \\ \Delta\eta_3 \\ \Delta\eta_4 \\ \Delta\eta_5 \\ \Delta\eta_6 \end{bmatrix} = \begin{bmatrix} p_{11} & p_{12} & p_{12} & 0 & 0 & 0 \\ p_{12} & p_{11} & p_{12} & 0 & 0 & 0 \\ p_{12} & p_{12} & p_{11} & 0 & 0 & 0 \\ 0 & 0 & 0 & \frac{1}{2}(p_{11}-p_{12}) & 0 & 0 \\ 0 & 0 & 0 & 0 & \frac{1}{2}(p_{11}-p_{12}) & 0 \\ 0 & 0 & 0 & 0 & 0 & \frac{1}{2}(p_{11}-p_{12}) \end{bmatrix} \begin{bmatrix} S_1 \\ S_2 \\ S_3 \\ S_4 \\ S_5 \\ S_6 \end{bmatrix} \tag{5}$$

Considering the change in the refractive index to be small, it can be written:

$$\Delta n_i = -\frac{n_0^3}{2}\Delta\eta_i. \tag{6}$$

The shear stress and strain components (σ_4, σ_5, σ_6 and S_4, S_5, S_6) are assumed to be negligible compared to the normal stress and strain components (σ_1, σ_2, σ_3 and S_1, S_2, S_3). Therefore, the following equations can be approximated for materials of a cubic crystal structure as well as isotropic materials. Using Hooke's law, the stress induced refractive index change for both, the cubic crystal structure and the isotropic material, now becomes:[19]

$$n_x \approx n_0 - C_1\sigma_x - C_2(\sigma_y + \sigma_z) \tag{7a}$$

$$n_y \approx n_0 - C_1\sigma_y - C_2(\sigma_z + \sigma_x) \tag{7b}$$

$$n_z \approx n_0 - C_1\sigma_z - C_2(\sigma_x + \sigma_y) \tag{7c}$$

with the constants

$$C_1 = \frac{n_0^3}{2E}(p_{11} - 2vp_{12}) \tag{8a}$$

$$C_2 = \frac{n_0^3}{2E}(-vp_{11} + (1-v)p_{12}) \tag{8b}$$

Here, v describes the Poisson ratio of the material and C_1 and C_2 are called stress-optic or photoelastic constants. They translate the strain-optic coupling described by the elements p_{ij} into a stress-optic coupling. It is worth noting that the spatial distribution of the strain tensor and not one single component is initiating the effective index change. The photoelastic constants are based on the approximation of an isotropic model of silicon. The validity of this assumption is verified by comparing the calculated stress components inside a silicon waveguide using the isotropic and the orthotropic model (Table 2). Values for the mechanical and photoelastic properties of silicon, silica and PDMS are summarized in Table 1.

Results

For each design approach, a simulation model is set-up considering the mechanical deformation of the membrane (A, B) and the waveguide and substrate (B, C) as well as the cladding (C). The change in effective refractive index of the waveguide is then found by carrying out a mode analysis. A SOI substrate with a silicon thickness of 220 nm and a BOX height of 2µm is assumed for all approaches. In the following, the results for each design approach are analyzed.

Free standing membrane (A)

A 2 µm thick SiO_2 membrane with a diameter of 20 µm is chosen for this study and simulated using the solid mechanics module in COMSOL. The simulation is carried out in 2D considering the cross section of the membrane in the center. The membrane layer is designed 24 µm wide and is mechanically constrained at each side and partially on the bottom by 2 µm wide support structures, which are placed directly below the membrane layer as indicated in Fig. 2 (b). This leads to a deflectable diameter of 20 µm. The deflection of the membrane surface for an applied external pressure is shown in Fig. 2 (a). A pressure of 1 Pa is chosen, which is also the targeted order of magnitude of the sensor's limit of detection. The deflection maximum at the membrane center is found to be 0.011 pm/Pa, which is comparable to the simulation results of Westerveld et al.[14] who used an acoustic pressure wave in the simulation instead of the static pressure applied in this study.

The derived relationship between pressure and membrane deflection will be used throughout the simulation study to calculate values of the sensitivity in RIU/Pa for approach A (Fig. 1). The same membrane geometry is used in design approach B, in which the membrane deflection directly influences the effective refractive index through the photoelastic effect. The use of the same membrane geometry allows a direct comparison of the theoretical sensitivity limitations of the two membrane based approaches. It must be mentioned that the relationship between pressure and membrane deflection can be applied only for low pressures leading to a linear behavior of the material. Furthermore, only constant pressures are considered in this study.

A mode analysis for design approach (A) is performed using the wave optics module in COMSOL. The model includes a silicon strip waveguide placed on top of the BOX and a SiO_2 membrane with a thin layer of silicon facing the waveguide. For the optical simulations, the thickness of the silicon layer (without the thick SiO_2 layer) will be referred to as the membrane thickness, since it is a crucial parameter influencing the effective refractive index. The membrane is placed above the waveguide with a varying gap distance between the waveguide and the membrane. The gap in between the waveguide and the membrane is filled with air. The model was validated using the results of Westerveld et al.[14] on the effective index change with a variation in gap height.

Figure 2 (c)-(f) shows the waveguide sensitivity values $\left|(\partial n_e/\partial g)\right|$ and $\left|(\partial n_e/\partial P)\right|$ of the TE and TM mode for different values of the gap height. Different waveguide widths (Fig. 2 (c)-(d)) and membrane thicknesses (Fig. 2 (e)-(f)) are considered. The sensitivity of the TM mode is found to reach sensitivity values over four times higher than the TE mode, but drops more rapidly for an enlargement of the gap height. In both cases smaller gap heights in between the waveguide and the membrane lead to higher values of the sensitivity. In the range of the waveguide widths and gap heights considered in the analysis, the TE mode is furthermore found to be dependent on the waveguide width, while the TM mode is not.

Property	Si	SiO_2	PDMS
Youngs modulus E (GPa)	130	76.7	0.75
Poisson ratio v	0.19	0.17	0.49
Refractive index n	3.4777	1.4657	1.3960
Photoelastic tensor element p_{11}	-0.101	0.16	-
Photoelastic tensor element p_{12}	0.0094	0.27	-
Photoelastic tensor constant C_1(TPa^{-1})	-17.13	1.17	-
Photoelastic tensor constant C_2(TPa^{-1})	5.51	3.73	-

Table 1. Mechanical, optical and photoelastic properties[20,21] of Si,[22] SiO_2[23] and PDMS[24]. The refractive index is given for a wavelength of 1550 nm and the photoelastic properties for a wavelength of 1150 nm as given in literature.

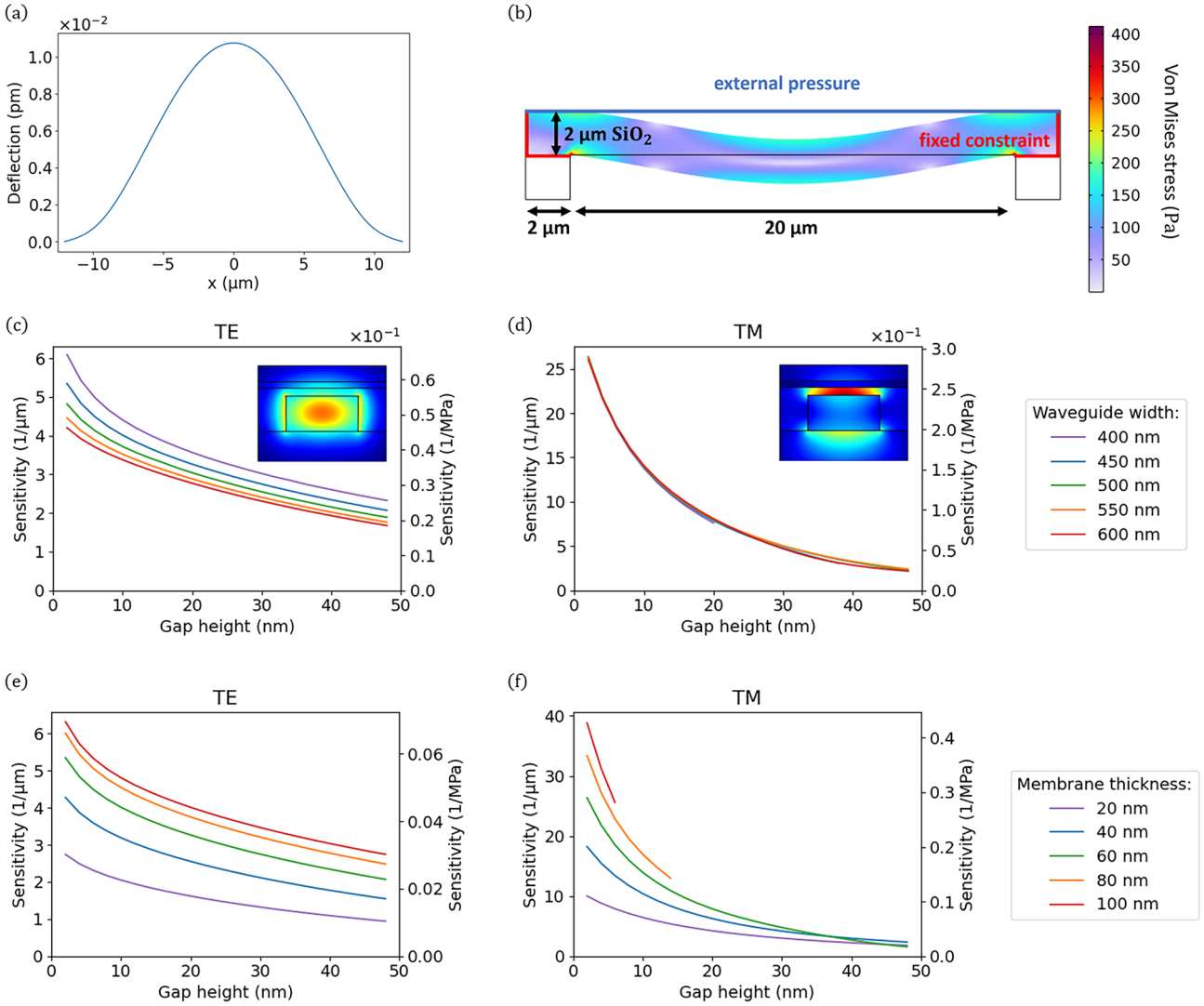

Fig. 2. (**a**) Calculated deflection of a SiO_2 membrane of 20 μm in diameter and 2 μm in height on top of silicon support structures. Each support structure has a width of 2 μm. An external pressure of 1 Pa is applied. (**b**) Simulation set-up, Von Mises stress and deflection of the membrane introduced by an external pressure (blue) of 1 Pa from the top surface. The deflection of the membrane is not drawn to scale. Fixed constraints are indicated in red. (**c**)-(**d**) Sensitivity over the gap height for different waveguide widths and (**e**)-(**f**) membrane thickness. The insets show the normalized electric field of the first order TE (**c**) and TM mode (**d**). In (**c**)-(**d**) the membrane is 60 nm thick and in (**e**)-(**f**) the waveguide width is 450 nm. The modes are solved for a wavelength of 1550 nm.

It is found, that a rise in membrane thickness in general causes higher sensitivities, but the influence saturates towards higher membrane thicknesses. A break-off point at a gap height around 10 nm for values of the membrane thickness above 60 nm is visible, where the mode is no longer supported by the structure.

Sensors with a waveguide width of 450 nm and a gap height of 15 nm, in combination with the above-described membrane geometry and a membrane thickness of 60 nm were already fabricated in proof-of-concept studies[14]. For this geometry, the performed simulations show a sensitivity of 3.52 RIU/μm or 0.04 RIU/MPa for the TE mode and a value of 9.74 RIU/μm or 0.11 RIU/MPa for the TM mode. The values given in RIU/MPa consider a placement of the waveguide in the center of the membrane. For the realization of the photonic sensor, the waveguide will most likely not be placed below the membrane center. This will reduce the sensitivity according to Fig. 2 (a).

In order to better understand the much higher sensitivity of the TM mode compared to the TE mode, for both modes the normalized field confinement factor is evaluated, which is defined as

$$\Gamma = \frac{\int_A \sqrt{P_x^2 + P_y^2 + P_z^2}\, dx\, dy}{\int_{-\infty}^{\infty} \sqrt{P_x^2 + P_y^2 + P_z^2}\, dx\, dy}. \tag{9}$$

P_x, P_y and P_z denote the electric field power in the x, y and z direction, respectively. The field confinement is determined inside of four different areas A: the strip waveguide, the membrane, the gap in between the waveguide and the membrane and a sum of all remaining areas. The field intensities are normalized with respect to the entire simulation domain.

Figure 3 (a) compares the normalized field confinement factors for a gap height of 15 nm, a waveguide width of 450 nm and a membrane thickness of 60 nm. For the TE as well as the TM mode, the electric field is mainly confined inside the waveguide structure. As to be expected, the confinement is stronger for the TE mode. For the TM mode the normalized field confinement inside the remaining areas is higher. Therefore, higher losses might be expected when the TM mode is used. However, in contrast to the TE mode, also the confinement inside the gap is much stronger for the TM mode. The field confinement for both modes is also evaluated over the gap height (Fig. 3 (b)-(e)). The course of the normalized field confinement factors each differs from the course of the sensitivity values (Fig. 2 (c)-(f)). Therefore, no direct impact from one component of the field confinement onto the sensitivity can be identified.

For the TE mode, it is found, that the course of the summed up normalized field confinement, of the waveguide and the membrane, which equals the course of the intensity in this areas, approximately matches the course of the sensitivity. The values are plotted in Fig. 3 (f). For the TM mode, the normalized intensity

$$I = \frac{\Gamma}{A} \tag{10}$$

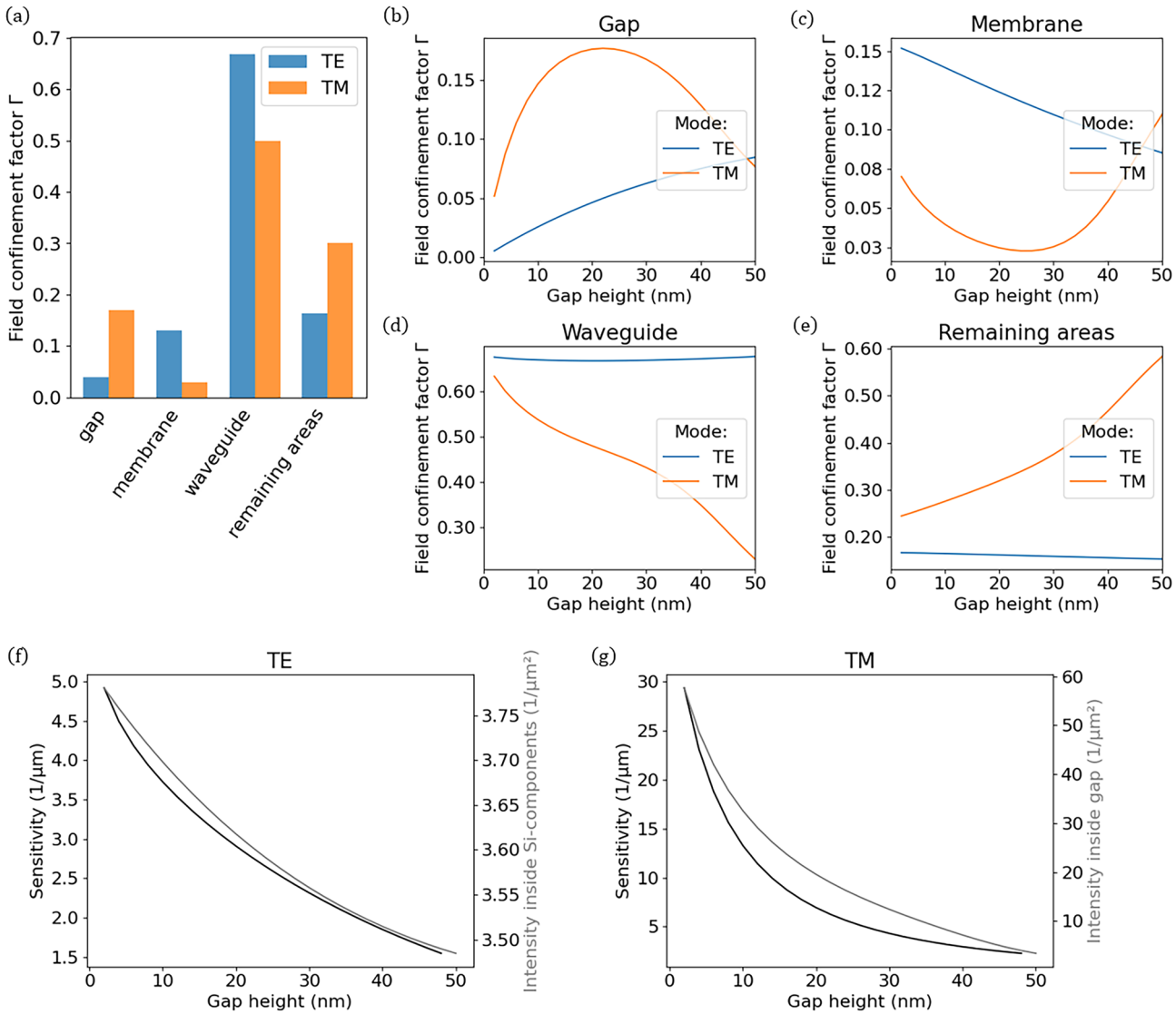

Fig. 3. (**a**) Field confinement factors for a gap height of 15 nm and a membrane thickness of 60 nm. (**b**)-(**e**) Field confinement factors of the TE and TM mode over the gap height. Sensitivity of the waveguide compared to the normalized intensity inside the silicon components (waveguide and membrane) for the TE mode (**f**) and inside the gap for the TM mode (**g**).

inside the gap approximately follows the course of the sensitivity curve as shown in Fig. 3 (g). Summarized, this indicates that the TM mode sensitivity is mainly influenced by the intensity inside the gap, while the TE mode sensitivity is mainly influenced by the intensity inside the silicon components (waveguide and membrane). The amount of light guided inside the latter (i.e. the field confinement) is in general much higher. On the other hand, the intensity inside the gap reaches very high values for the TM mode, as the light is confined inside a very small area.

For completeness, the study is repeated for a slot waveguide geometry. The results show lower sensitivity values of 0.02 RIU/MPa and 0.11 RIU/MPa for the TE and TM mode, respectively.

Waveguide on top of membrane (B)

For approach B, a COMSOL stress-optical model of a waveguide on top of the membrane is set-up. For the SiO_2 membrane the geometry described for approach A is chosen (Fig. 2 (b)). The solid mechanics module is used to estimate the deformation of the membrane and the waveguide by an external pressure from the top and the induced mechanical stress. Linear behavior of the material is assumed. The mechanical properties of Si are modeled as isotropic instead of orthotropic, as there is a minimal difference in the resulting stress values (Table 2).

The stress distribution in the waveguide region is shown in Fig. 4 (a-c) for an applied pressure of 1 Pa. The refractive index changes of the materials are related to the determined material stress by the photoelastic effect, as explained above (equation 7). In a second simulation step, an electromagnetic mode solver is used to find the effective refractive index of the waveguide.

The sensitivity over the waveguide width is analyzed for a strip waveguide surrounded by air and a waveguide with an additional 1.5 µm thick SiO_2 cladding (Fig. 4 (d)-(e)). The latter might be referred to as a waveguide embedded into the membrane. In both cases the waveguide is positioned at the center of the membrane surface. The waveguide surrounded by air shows a higher sensitivity, which is caused by a stronger deflection of the membrane due to a lower thickness. Furthermore, the waveguide is positioned on the membranes surface, if no cladding is applied, where the highest stresses are found. For the TE mode an increase in the waveguide width causes a rise of the sensitivity, while for the TM mode this behavior is not observed. In contrast, the sensitivity of the TM mode slightly decreases for large waveguide widths.

The same methods are applied for a slot waveguide (Fig. 4 (f)-(g)). In this case, the slot width is changed. While the TM mode shows comparable sensitivity, the TE mode sensitivity is almost one order of magnitude lower compared to the strip waveguide geometry. In the strip waveguide, the TE mode is mainly guided inside of air or the SiO_2 cladding with a lower photoelastic coupling than silicon. The TE and TM mode sensitivity values of the slot waveguide are comparable. This is explained by comparable field confinement factors inside the membrane (Table 3).

The strip waveguide sensitivity is derived for different radial displacements from the center of the membrane. The results are plotted in Fig. 4 (h)-(i). Besides the sensitivity of the entire waveguide geometry, also the effective index change caused by the photoelastic effect inside the silicon waveguide and inside the SiO_2 membrane are shown (dashed lines). It is found that the TE mode is mainly influenced by the photoelastic effect inside the silicon waveguide. This effect is weakened by the SiO_2 membrane due to the opposite signs of the photoelastic constant C_1. For the TM mode on the other hand, the effective index change mainly arises from the photoelastic effect inside the SiO_2 membrane. In this polarization direction the photoelastic effects inside of silicon and SiO_2 are causing an increase in refractive index due to the addition of both photoelastic constants C_1.

The results also explain the relationship between sensitivity and waveguide width for the TE and TM mode. A wider waveguide leads to stronger confined TE mode inside the waveguide core, which increases the interaction between the light and the stress inside the silicon waveguide. The TM mode sensitivity does not show a strong dependence on the waveguide width, as the mode is mainly guided inside the substrate and cladding.

The simulation is repeated with a mechanically constrained substrate to discretize the influence of the membrane and waveguide deformation. The pressure deforming only the silicon waveguide does lead to effective refractive index changes of the TE and TM mode of $\Delta n_{TE} = -3 \cdot 10^{-6} \mathrm{RIU/MPa}$ and $\Delta n_{TM} = -1 \cdot 10^{-6} \mathrm{RIU/MPa}$, respectively. This is one order of magnitude smaller than the derived effective index change with a deflected membrane. Even though the TE mode refractive index change does mainly depend on the photoelastic effect inside of the silicon waveguide, the membrane deflection is needed to strongly enhance the stress inside the waveguide and therewith the photoelastic refractive index change.

Polymer cladding (C)

A stress-optical model is set up, which includes a mechanically constrained SiO_2 substrate (BOX), a silicon waveguide and a polymer cladding covering the waveguide. A static pressure is evenly applied from above the polymer cladding, which mechanically deforms the polymer cladding and the waveguide. The thickness of the polymer cladding is chosen high enough to expand all the way to the end of the domain, in which the

modelling approach	$\int_{WG} \sigma_x dA$[N]	$\int_{WG} \sigma_y dA$[N]	$\int_{WG} \sigma_z dA$[N]
isotropic	-6.20e-13	-9.90e-14	-1.37e-13
orthotropic	-6.71e-13	-9.90e-14	-1.52e-13

Table 2. Comparison of resulting stress inside a silicon waveguide for isotropic and orthotropic silicon modelling. Each stress component is integrated over the area A of the waveguide (WG) cross section.

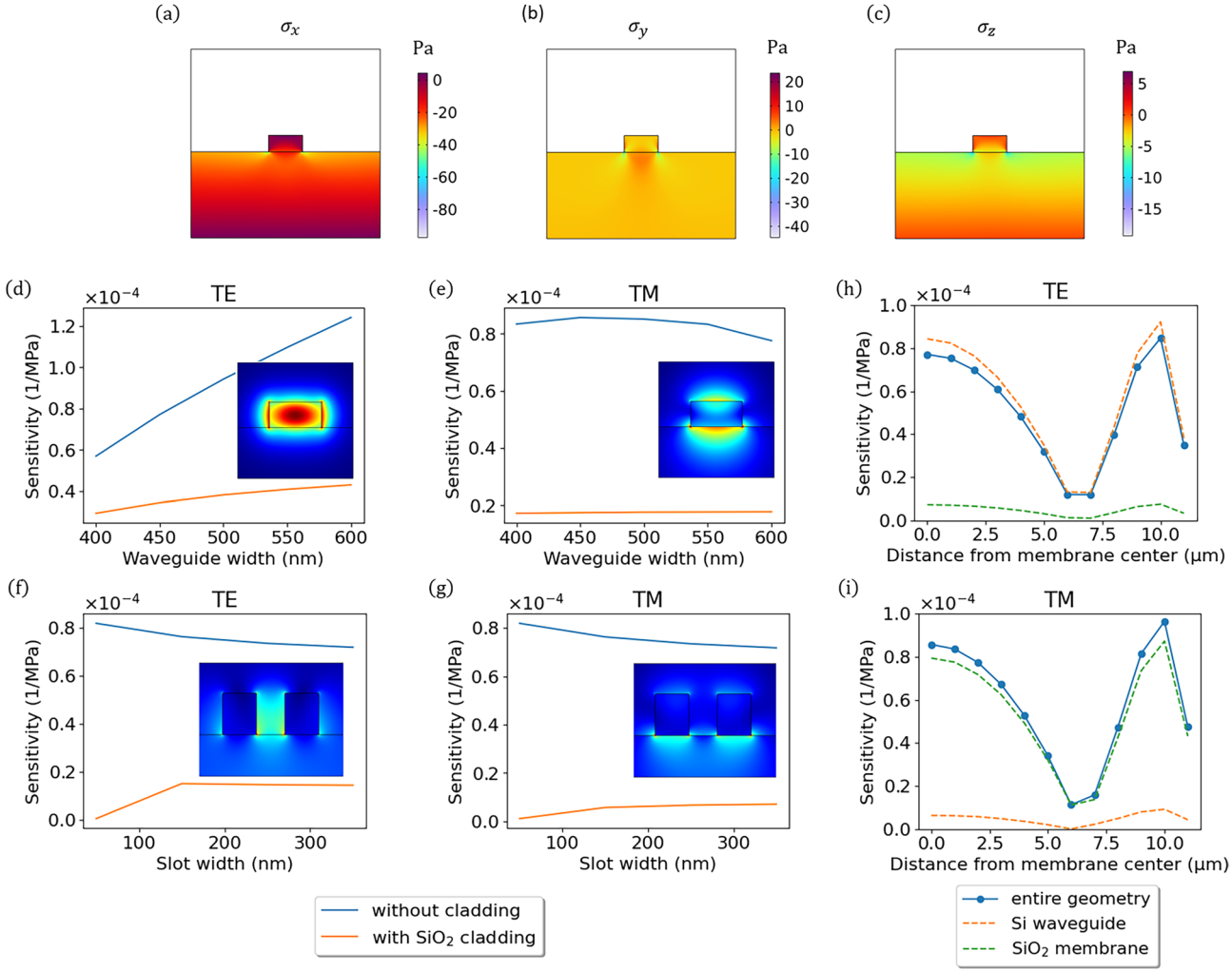

Fig. 4. (**a**)-(**c**) Stress components inside waveguide and surrounding. (**d**)-(**g**) Sensitivity over waveguide width for a waveguide surrounded by air and a waveguide embedded into an additional SiO_2 cladding. The values are shown for a strip (**d**)-(**e**) and a slot waveguide (**f**)-(**g**). The width of the two silicon parts of the slot waveguide is 180 nm. The insets show the normalized electric field inside the waveguide, respectively. (**h**)-(**i**) Sensitivity over waveguide displacement on the membrane surface for TE (**h**) and TM (**i**) mode. Dashed lines are showing the results for solving the equations of the photoelastic effect only inside the silicon waveguide (orange) or only inside the SiO_2 membrane (green).

Waveguide	Mode	$\Gamma_{membrane}$	Γ_{Si}
Strip	TE	0.12	0.79
	TM	0.58	0.31
Slot	TE	0.81	0.03
	TM	0.84	0.06

Table 3. Field confinement factors inside the membrane and the waveguide for a waveguide width of 450 nm for the strip waveguide and a slot width of 150 nm for the slot waveguide. For both waveguides an air surrounding is considered.

electromagnetic modes are solved. The stress distribution in the waveguide region is shown in Fig. 5 (a)-(c) for an applied pressure of 1 Pa. The calculated stress values are again coupled to the refractive indices of the silicon waveguide and the polymer cladding by Eq. 7.

PDMS is chosen as an example polymer, because it is known to exhibit a large photoelastic response and overall compatibility with silicon based materials. Furthermore, a photonic ultrasound sensor based on a PDMS cladding has already been experimentally demonstrated.[16] The photoelastic constants are given as a difference

$C_1 - C_2 > 10^3 \mathrm{TPa}^{-1}$ in literature.[17] Therefore, two different combinations are chosen for the simulation. Both combinations lead to the conservative assumption of $C_1 - C_2 = 10^3 \mathrm{TPa}^{-1}$.

Figure 5 shows the effective refractive index change, induced by an applied pressure, for a strip (d)-(e) and a slot waveguide (e)-(f). The sensitivity in this approach (C) is one order of magnitude higher than the sensitivity of the previously described approach (B). This is due to the strong photoelastic response of the cladding.

It is observed that the sensitivity of the TM mode is about twice as high as the sensitivity of the TE mode. This is expected due to the stronger confinement of the TE mode inside the silicon waveguide, reducing interaction with the surrounding. For a slot waveguide on the other hand, also the TE mode shows comparable sensitivity values (Fig. 5 (e)), as the light is guided inside the polymer filled slot leading to a strong interaction with the cladding. This relationship is already known from different SOI based sensors, e.g. biosensors.[25] Also in this approach the field confinement inside the cladding and hence the waveguide sensitivity are comparable for the TE and TM mode inside the slot waveguide (Table 4).

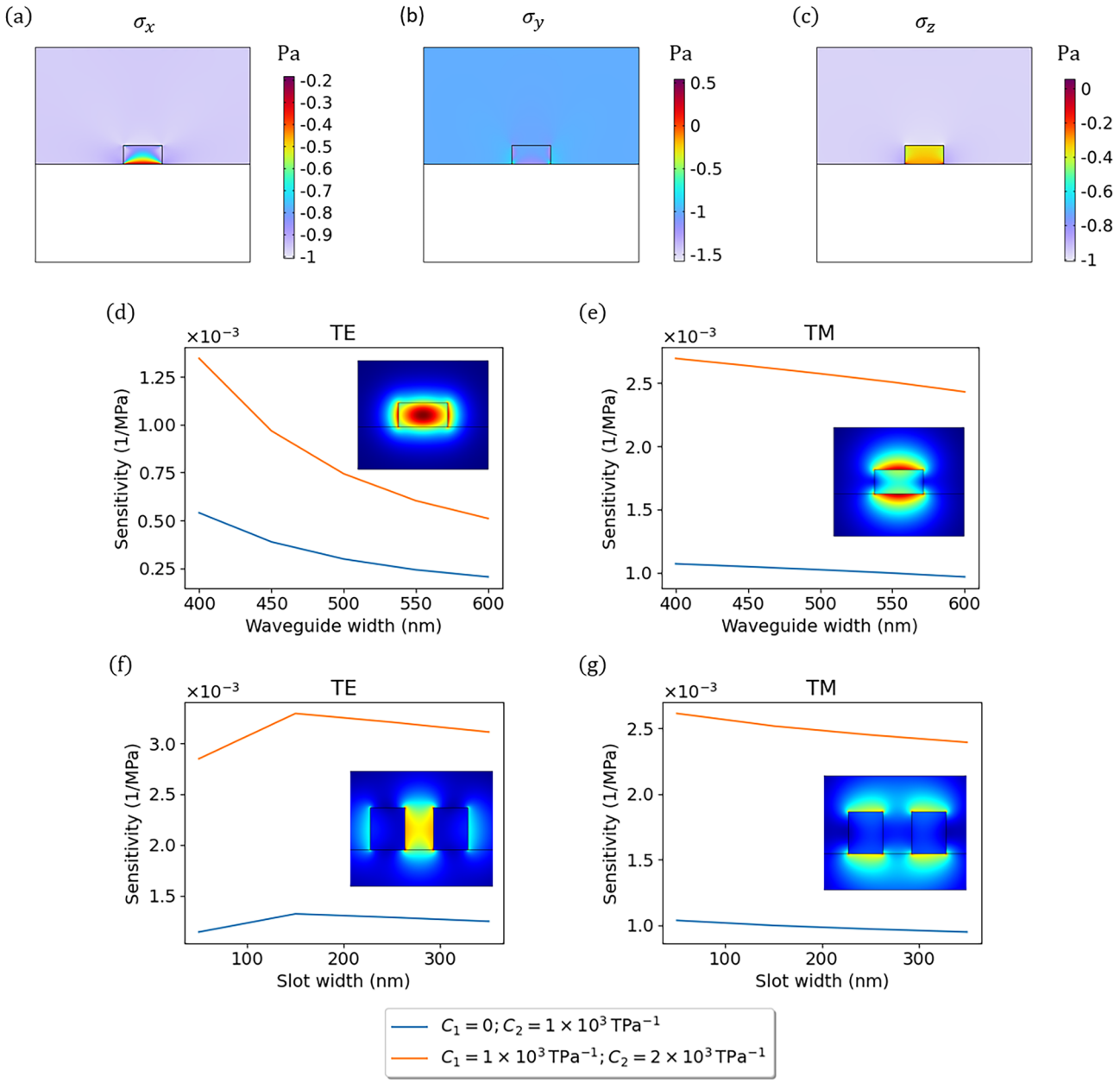

Fig. 5. (**a**)-(**c**) Stress components inside waveguide surrounding. (**d**)-(**g**) Sensitivity over waveguide width and slot width for a silicon waveguide covered by a PDMS cladding. Two different combinations of the photoelastic constants C_1 and C_2 are considered. The values are shown for a strip (**d**)-(**e**) and a slot waveguide (**f**)-(**g**). The insets show the normalized electric field inside the waveguide, respectively.

Waveguide	Mode	$\Gamma_{cladding}$	Γ_{Si}
Strip	TE	0.15	0.75
	TM	0.43	0.42
Slot	TE	0.54	0.11
	TM	0.42	0.15

Table 4. Field confinement factors inside the cladding and the waveguide for a waveguide width of 450 nm for the strip waveguide and a slot width of 150 nm for the slot waveguide.

Material	λ(nm)	h_{WG}(nm)	w_{WG}(nm)	(A) membrane height (nm)
Si	1550	220	450	60
Si_3N_4	1550	300	1500	100
	850	300	450	100

Table 5. Selected waveguide geometries for the comparison of the three different approaches. For approach (B) the air surrounding of the waveguide is selected.

Discussion

Three different two-dimensional SOI-based waveguide design approaches (see Fig. 1) are analyzed within this simulation study. A FEM simulation for each design is set-up and the effective refractive index change due to a constant applied pressure is carried out for the TE and TM mode inside a strip and a slot waveguide, respectively. The study is also conducted for silicon nitride strip waveguides (see Appendix, Figures S1-S6). For both materials a waveguide geometry for the comparison of all approaches is chosen as summarized in Table 5. Besides the waveguide sensitivity also a sensitivity value of an example geometry for a micro-ring resonator (MRR) is calculated.

$$S_{MRR} = \frac{\lambda_{res}}{n_g} \cdot S_{WG} = \frac{\lambda_{res}}{n_g} \cdot \frac{\partial n_{eff}}{\partial P} \tag{11}$$

λ_{res} and n_g are the resonant and the group index of the waveguide, respectively. The MRR geometry is chosen such that the device footprint does not exceed a size of 20 µm. For approach (A) a membrane radius of 10 µm is chosen and a MRR radius of 5 µm. While smaller radii increase the sensitivity, this choice ensures no significant bending losses for silicon waveguides. For approach (B) a radius of 10 µm is chosen, because high sensitivity values are reached at the membrane center as well as the membrane boundary. The sensitivity of approach (C) is independent of the MRR radius. Table 6 gives an overview of the waveguide sensitivities and MRR sensitivities.

Design approach (A), relying on a geometrical change of the waveguide structure, incorporates a free standing membrane above the waveguide with a minimal gap in between the two components. While this design approach is most challenging in fabrication, outstanding sensitivity values are observed. So far, this waveguide design was only reported for the use of the TE mode. This simulation study indicates that the TM mode shows a sensitivity almost three times higher, due to a strong enhancement of the field confinement inside the gap. Also the field confinement inside the remaining (not light guiding) structures is enhanced, which will lead to higher losses of the TM mode. It should be investigated to what extent the losses reduce the sensor performance. So far, a successful fabrication of this design approach was demonstrated by wafer-to-wafer bonding of a SOI wafer with waveguide and spacer structures towards another wafer, which is afterwards thinned down to obtain the membrane. This approach is not compatible with the incorporation of a back end of line (BEOL) yet.

Design approach (B) uses the BOX as a membrane with a silicon waveguide on top. Such a structure can be fabricated by local backside etching of the silicon substrate. An integration of a BEOL, as demonstrated by Zarkos,[13] leads to a lowering of the sensitivity due to the change in membrane properties. This approach shows the lowest sensitivity, caused by weak elasto-optic response of the used materials. However, the processing of these sensors is comparable simple, since local backside etching is a well-known process in photonic integrated circuit technologies.[26,27]

Design approach (C) uses a polymer cladding of a material of high photoelastic response (here PDMS) on top of the waveguide. Since this approach is not relying on an acoustical membrane, the acoustic and optic response of the sensor are not coupled to the membrane geometry. A high bandwidth of the sensor is expected. The values listed in table 6 consider the choice of C_1 and C_2 of 0 and $10^3 \mathrm{TPa}^{-1}$. The photoelastic constants of the simulated PDMS cladding were chosen conservatively, as only a minimum value for the difference $C_1 - C_2$ is given in literature. The resulting sensitivity values of the structure are already higher than in approach B. By using a slot waveguide, the TE mode sensitivity is enhanced by almost one order of magnitude. Moreover, this approach offers the possibility of full EPIC integration with a BEOL. This might be achieved by etching a window from the top or local backside etching of the substrate and a removal of the BOX. The etched window could subsequently be filled with the polymer.

The simulations were performed under the following assumptions: the set membrane geometry (approach A, B), a linear mechanical behavior of the materials (approach A, B, C), the choice of PDMS as a cladding

Approach	Material	$\lambda(\mathrm{nm})$	Mode	n_{eff}	n_g	S_{WG} (RIU/MPa)	S_{MRR} (nm/MPa)
(A)	Si	1550	TE	2.5246	4.0359	2.46×10^{-2}	9.45
			TM	1.9218	3.8206	6.82×10^{-2}	2.77×10^{1}
	Si_3N_4	1550	TE	1.8255	2.2140	6.32×10^{-3}	4.42
			TM	1.6560	2.0900	1.89×10^{-2}	1.40×10^{1}
		850	TE	1.8490	3.3208	9.43×10^{-3}	3.45
			TM	1.7910	2.2925	1.73×10^{-2}	6.41
(B)	Si	1550	TE	2.2999	4.4079	8.48×10^{-5}	2.98×10^{-2}
			TM	1.5724	3.2697	9.65×10^{-5}	4.57×10^{-2}
	Si_3N_4	1550	TE	1.7071	2.2186	2.80×10^{-6}	1.96×10^{-3}
			TM	-	-	-	-
		850	TE	1.7706	2.4294	7.50×10^{-6}	2.62×10^{-3}
			TM	1.7099	2.4324	3.28×10^{-5}	1.15×10^{-2}
(C)	Si	1550	TE	2.4253	4.0528	3.88×10^{-4}	1.48×10^{-1}
			TM	1.8901	3.5021	1.05×10^{-3}	4.65×10^{-1}
	Si_3N_4	1550	TE	1.6586	2.0229	3.72×10^{-4}	2.85×10^{-1}
			TM	1.5387	1.8410	6.27×10^{-4}	5.28×10^{-1}
		850	TE	1.7129	2.1762	3.98×10^{-4}	1.55×10^{-1}
			TM	1.6718	2.1606	4.46×10^{-4}	1.75×10^{-1}

Table 6. Comparison of the resulting sensitivity values for strip waveguides with a silicon and silicon nitride core. The sensitivity values are given for MRR diameters of 5 µm (A) and 10 µm (B). The waveguide as well as MRR sensitivity is independent of the MRR diameter for approach (C).

material (approach C) and the values of the elasto-optic coefficients of PDMS (approach C). Therefore, the calculated values should be handled accordingly. The calculated trend in device sensitivity matches the literature values[12,14,16] listed in the introduction. For approach A and C, the wavelength shift of the resonance curve (in this study S_{MRR}) for comparable device designs is also found in literature. In both cases, the measured sensitivities of 35 $\mathrm{nmMPa^{-1}}$ and 0.9 $\mathrm{nmMPa^{-1}}$ are higher than the calculated values of 9.45 $\mathrm{nmMPa^{-1}}$ and 0.29 $\mathrm{nmMPa^{-1}}$ for approach A and C, respectively. For the latter, this difference could be explained by the conservative choice of C_1 and C_2 in this study. The assumption of a linear mechanical behavior of the materials is appropriate considering the typically applied pressures of a few kilopascals in photoacoustic imaging applications.[28]

The results give a good comparison of the different approaches, which until now were not considered in experimental studies in literature, because the final device sensitivity depends on different aspects of the device layout and measurement set-up. Even with a standardized device approach and set-up it will still be challenging to obtain comparable results for different approaches, since the interactions with the mechanical element (membrane or cladding) might differ, e.g. a change in bending losses or coupling efficiency. Therefore, the simulation-based approach is an important step towards the selection of a suitable waveguide geometry for future developments of photonic integrated ultrasound sensors.

The sensitivity of the example MRR configuration is calculated under the assumption of dispersive coupling. The considered approaches could also introduce dissipative coupling by a change in coupling conditions at the MRR coupler region. For the studied designs (Approaches A, B and C) and analyzed parameters (waveguide and MRR sensitivity for an example MRR geometry), the SOI platform proofs a suitable design foundation for highly miniaturized ultrasound sensors. Silicon nitride waveguides lead to a slight decrease in sensitivity for approach A and B and a slight increase in sensitivity for approach C. Considering the enlarged bending losses for SiN waveguides, the increase in sensitivity comes along with a decrease in quality factor for small footprint MRR.

Summary

In this work a systematic simulation study is carried out using FEM of different pressure sensitive SOI-based waveguide architectures: (A) A flexibel silicon membrane above a silicon waveguide, (B) a silicon waveguide on top of a SiO_2 membrane (BOX) and (C) a silicon waveguide covered by a PDMS cladding with high photoelastic coefficients. All waveguide approaches can be incorporated into an ultrasound detecting structure e.g. for the use as a detector in photoacoustic imaging applications. Approach A relies mainly on the geometrical change of the waveguide structure with an applied pressure. The latter two approaches detect pressure through the photoelastic effect, which describes the refractive index change due to stress introduced into the material.

For all approaches a simulation is set-up taking into account the mechanical deformation of the structure as well as the change in effective refractive index of the waveguide by performing a two-dimensional mode analysis. A strip as well as a slot waveguide are systematically analyzed for the first-order TE and TM mode, respectively. It is observed, that design approach (A) offers the highest sensitivity limit with a value of 0.04 RIU/MPa and 0.11 RIU/MPa for the TE and TM mode for the considered membrane deflection at the membrane center. The high sensitivity of the TM mode is found to be caused by a high field confinement of the mode inside of the gap in between the waveguide and the membrane. The usage of the TM mode in combination with

a free-movable membrane above a silicon strip waveguide has not been reported so far. It will be necessary to measure the waveguide losses experimentally, to find out, if the the higher waveguide sensitivity can account for the additional losses caused by the overall less confined field of the TM mode. Design approach (B) on the other hand shows the lowest sensitivity with values of $7.18 \cdot 10^{-5}$ RIU/MPa and $8.59 \cdot 10^{-5}$ RIU/MPa for the TE and TM mode inside a strip waveguide at the membrane center. For design approach (C), sensitivity values of $3.88 \cdot 10^{-3}$ RIU/MPa and $1.05 \cdot 10^{-3}$ RIU/MPa are approximated for a strip waveguide. Our study suggests that the sensitivity can be enhanced by almost one order of magnitude, using the TM mode inside a strip waveguide or the TE mode inside a slot waveguide. The simulation study is repeated for silicon nitride waveguides. For approach (A) and (B) the sensitivity is slightly lowered and for approach (C) the sensitivity is slightly increased by using silicon nitride instead of silicon waveguides.

By systematically evaluating and comparing the key cross-sectional designs, this work provides an essential foundation for the development of miniaturized ultrasound photonic sensors with enhanced sensitivity. The underlying design insights will guide future endeavors to push the limits of sensitivity, bandwidth, and array integration, thereby expanding the capabilities of photonic pressure sensors in biomedical imaging and other ultrasound sensing applications.

Data availability

The datasets used and/or analysed during the current study available from the corresponding author on reasonable request.

Received: 13 September 2024; Accepted: 9 May 2025
Published online: 20 June 2025

References

1. Wissmeyer, G., Pleitez, M. A., Rosenthal, A. & Ntziachristos, V. Looking at sound: optoacoustics with all-optical ultrasound detection. *Light: Science & Applications* **7**, 53 (2018).
2. Thomson, J., Wickramasinghe, H. & Ash, E. A fabry-perot acoustic surface vibration detector-application to acoustic holography. *J. Phys. D. Appl. Phys.* **6**, 677 (1973).
3. Rousseau, G., Gauthier, B., Blouin, A. & Monchalin, J.-P. Non-contact biomedical photoacoustic and ultrasound imaging. *J. Biomed. Opt.* **17**, 061217. https://doi.org/10.1117/1.JBO.17.6.061217 (2012).
4. Beard, P., Perennes, F. & Mills, T. Transduction mechanisms of the fabry-perot polymer film sensing concept for wideband ultrasound detection. *IEEE Trans. Ultrason. Ferroelectr. Freq. Control.* **46**, 1575–1582. https://doi.org/10.1109/58.808883 (1999).
5. Wild, G. & Hinckley, S. Acousto-ultrasonic optical fiber sensors: Overview and state-of-the-art. *IEEE Sensors Journal* **8**, 1184–1193. https://doi.org/10.1109/JSEN.2008.926894 (2008).
6. Atique, S. et al. Detecting ultrasound using optical fibres. *J. Opt.* **33**, 241–255 (2004).
7. Li, H., Dong, B., Zhang, Z., Zhang, H. F. & Sun, C. A transparent broadband ultrasonic detector based on an optical micro-ring resonator for photoacoustic microscopy. *Sci. Rep.* **4**, 4496 (2014).
8. Gallego, D., Wang, M., Hiltunen, J., Myllylä, R. & Lamela, H. Polymer inverted-rib optical waveguide interferometric sensor for optoacoustic imaging. In editorOraevsky, A. A. & editorWang, L. V. (eds.) *booktitlePhotons Plus Ultrasound: Imaging and Sensing 2012*, vol. 8223, 822343, https://doi.org/10.1117/12.910826. organizationInternational Society for Optics and Photonics (publisherSPIE, 2012).
9. Chao, C.-Y., Ashkenazi, S., Huang, S.-W., O'Donnell, M. & Guo, L. J. High-frequency ultrasound sensors using polymer microring resonators. *IEEE Trans. Ultrason. Ferroelectr. Freq. Control.* **54**, 957–965. https://doi.org/10.1109/TUFFC.2007.341 (2007).
10. Ling, T., Chen, S.-L. & Guo, L. J. Fabrication and characterization of high q polymer micro-ring resonator and its application as a sensitive ultrasonic detector. *Opt. Express* **19**, 861–869. https://doi.org/10.1364/OE.19.000861 (2011).
11. Rosenthal, A. et al. Embedded ultrasound sensor in a silicon-on-insulator photonic platform. *Applied Physics Letters* **104** (2014).
12. Leinders, S. M. et al. A sensitive optical micro-machined ultrasound sensor (omus) based on a silicon photonic ring resonator on an acoustical membrane. *Sci. Rep.* **5**, 14328 (2015).
13. Zarkos, P. & Stojanovic, V. *Realization of a Fully Integrated Electronic-Photonic Sensor-Receiver Array for Endoscopic Ultrasound*. Ph.D. thesis, schoolUC Berkeley (2021).
14. Westerveld, W. J. et al. Sensitive, small, broadband and scalable optomechanical ultrasound sensor in silicon photonics. *Nat. Photonics.* **15**, 341–345 (2021).
15. Ding, Z., Sun, J., Li, C. & Shi, Y. Broadband ultrasound detection using silicon micro-ring resonators. *J. Lightwave. Technol.* **41**, 1906–1910 (2022).
16. Nagli, M. et al. Silicon photonic acoustic detector (spade) using a silicon nitride microring resonator. *Photoacoustics* **32**, 100527. https://doi.org/10.1016/j.pacs.2023.100527 (2023).
17. Angioletti, A., Eccher, S., Polvara, O. & Zerbini, V. Rubber birefringence and photoelasticity. *Rubber Chemistry and Technology* **38**, 1115–1163 (1965).
18. Yariv, A. & Yeh, P. *Optical waves in crystals*, vol. 5 (publisherWiley New York, 1984).
19. Theocaris, P. S. & Gdoutos, E. E. *Matrix theory of photoelasticity*, vol. 11 (publisherSpringer, 2013).
20. Tsesses, S., Aronovich, D., Grinberg, A., Hahamovich, E. & Rosenthal, A. Modeling the sensitivity dependence of silicon-photonics-based ultrasound detectors. *Optics letters* **42**, 5262–5265 (2017).
21. Ye, W. N. et al. Birefringence control using stress engineering in silicon-on-insulator (soi) waveguides. *J. Lightwave. Technol.* **23**, 1308–1318 (2005).
22. Salzberg, C. D. & Villa, J. J. Infrared refractive indexes of silicon germanium and modified selenium glass. *JOSA* **47**, 244–246 (1957).
23. Lemarchand, F. private communications (2013). index determination is performed using method explained in: L. gao, f. lemarchand, and m. lequime. comparison of different dispersion models for single layer optical thin film index determination. *Thin Solid Films* **520**, 501–509 (2011).
24. Querry, M. R. *Optical constants of minerals and other materials from the millimeter to the ultraviolet* (publisherChemical Research, Development & Engineering Center, US Army Armament 1998).
25. Steglich, P. et al. Silicon photonic micro-ring resonators for chemical and biological sensing: A tutorial. *IEEE Sensors Journal* **22**, 10089–10105. https://doi.org/10.1109/JSEN.2021.3119547 (2022).
26. Mai, C., Steglich, P., Fraschke, M. & Mai, A. Back-side release of slot waveguides for the integration of functional materials in a silicon photonic technology with a full beol. *IEEE Trans. Compon. Packaging. Manuf. Technol.* **10**, 1569–1574. https://doi.org/10.1109/TCPMT.2020.3011149 (2020).

27. Adamopoulos, C. et al. Lab-on-chip for everyone: Introducing an electronic-photonic platform for multiparametric biosensing using standard cmos processes. *IEEE Open Journal of the Solid-State Circuits Society* **1**, 198–208. https://doi.org/10.1109/OJSSCS.2021.3118336 (2021).
28. Fu, B. et al. Optical ultrasound sensors for photoacoustic imaging: a narrative review. *Quant. Imaging. Med. Surg.* **12**, 1608 (2022).

Acknowledgements
This work was funded by the Federal Ministry of Education and Research (BMBF) under agreement no. 16ME0870.

Author contributions
T.F. conducted simulations, T.F. and P.S. developed the methodology and the theory, M.P. and C.M. and P.S. analyzed the results. C.W. and A.M. reviewed the manuscript.

Declarations

Competing interests
The authors declare no competing interests.

Additional information
Supplementary Information The online version contains supplementary material available at https://doi.org/10.1038/s41598-025-01953-9.

Correspondence and requests for materials should be addressed to T.F.

Reprints and permissions information is available at www.nature.com/reprints.

Publisher's note Springer Nature remains neutral with regard to jurisdictional claims in published maps and institutional affiliations.